SCIENTIFIC REPORTS

OPEN

SUBJECT AREAS:
ORGANIC LEDS
NANOPHOTONICS AND PLASMONICS
PHOTONIC CRYSTALS
SOLAR CELLS

Received
19 August 2013

Accepted
24 January 2014

Published
10 February 2014

Correspondence and requests for materials should be addressed to J.-X.T. (jxtang@suda.edu.cn); Y.-Q.L. (yqli@suda.edu.cn) or S.-T.L. (apannale@suda.edu.cn)

* These authors contributed equally to this work.

Light Manipulation for Organic Optoelectronics Using Bio-inspired Moth's Eye Nanostructures

Lei Zhou[1]*, Qing-Dong Ou[1]*, Jing-De Chen[1]*, Su Shen[2], Jian-Xin Tang[1], Yan-Qing Li[1] & Shuit-Tong Lee[1]

[1]Jiangsu Key Laboratory for Carbon-Based Functional Materials & Devices, Institute of Functional Nano & Soft Materials (FUNSOM), and Collaborative Innovation Center of Suzhou Nano Science and Technology, Soochow University, Suzhou 215123, China, [2]Institute of Information Optical Engineering, Soochow University, Suzhou 215006, China.

Organic-based optoelectronic devices, including light-emitting diodes (OLEDs) and solar cells (OSCs) hold great promise as low-cost and large-area electro-optical devices and renewable energy sources. However, further improvement in efficiency remains a daunting challenge due to limited light extraction or absorption in conventional device architectures. Here we report a universal method of optical manipulation of light by integrating a dual-side bio-inspired moth's eye nanostructure with broadband anti-reflective and quasi-omnidirectional properties. Light out-coupling efficiency of OLEDs with stacked triple emission units is over 2 times that of a conventional device, resulting in drastic increase in external quantum efficiency and current efficiency to 119.7% and 366 cd A^{-1} without introducing spectral distortion and directionality. Similarly, the light in-coupling efficiency of OSCs is increased 20%, yielding an enhanced power conversion efficiency of 9.33%. We anticipate this method would offer a convenient and scalable way for inexpensive and high-efficiency organic optoelectronic designs.

The external quantum efficiency (EQE) of an organic optoelectronic device is generally EQE = LCE × IQE[1–10]. Here, the internal quantum efficiency (IQE) is the probability of the electron–photon conversion in the active regions. The light coupling efficiency (LCE) is the fraction of emitted light that is out-coupled from OLEDs to the air, or incident light that is in-coupled by absorption in the active layer of OSCs. Currently, an IQE of nearly 100% has been realized in OLEDs with phosphorescent materials using both singlet and triplet states[4,11–13], while efficiency improvement in OSCs is chiefly achieved via optimization of exciton dissociation and charge collection[6,10,14]. Nevertheless, the LCE for conventional OLEDs is still limited to ~20% due to optical confinement and internal reflection by the high refractive index of organic materials and glass substrate[15–18]. Similarly, due to mismatch between optical absorption length and charge transport scale in OSCs, a large fraction of incident light remains wasted for photocurrent generation, limiting EQE and thus power conversion efficiency (PCE)[6,9,19–23]. Therefore, a substantial improvement in overall device efficiency for organic optoelectronics can be readily achieved via optimal light manipulation in the photo-active regions[1–3,6,7,24].

Various photonic structures have been implemented in the appropriate interfaces for guiding and retaining light within the active regions of OLEDs and OSCs, such as the use of low-index dielectric grid[2,28], high refractive index substrate[1], subwavelength photonic crystals[25–27], microlens arrays[29–31], optical spacers[32,33], optical cavities[34,35], wrinkles[7], spontaneously formed buckles[3], or metallic nanostructures-induced plasmonic effect[3,23,27,36–40]. Often, those reported methods for light manipulation are hindered for practical adoption due to undesirable spectral distortion or shifting, response at specific light wavelengths or complicated fabrication process.

It is well-known that biological systems in nature possess amazing ability in manipulation of light propagation via unique nanostructured surfaces. Particularly, biomimetic moth's eye nanostructure (MEN) with a two-dimensional sub-wavelength structure can exhibit unique optical properties in suppressing the Fresnel reflections at an interface, yielding high transmittance over a broad spectral range and wide angles of incidence[41–46]. Here we introduce a universal method for efficient light manipulation in OLEDs and OSCs by integrating a dual-side MEN through nanoimprint lithography, as shown in Fig. 1a. The present MEN has the great advantage of facile manufacturing compatibility for large-area and low-cost electronic devices, and is especially suitable for light manipulation with broad spectral response and directional randomness. The OLED device constructed with the MENs shows a remarkable improvement in LCE of more than 2 times. The maximum EQE and current efficiency of a MEN-patterned green phosphorescent OLED are increased to 119.7% and 366 cd A^{-1} at 1,000 cd m^{-2} with

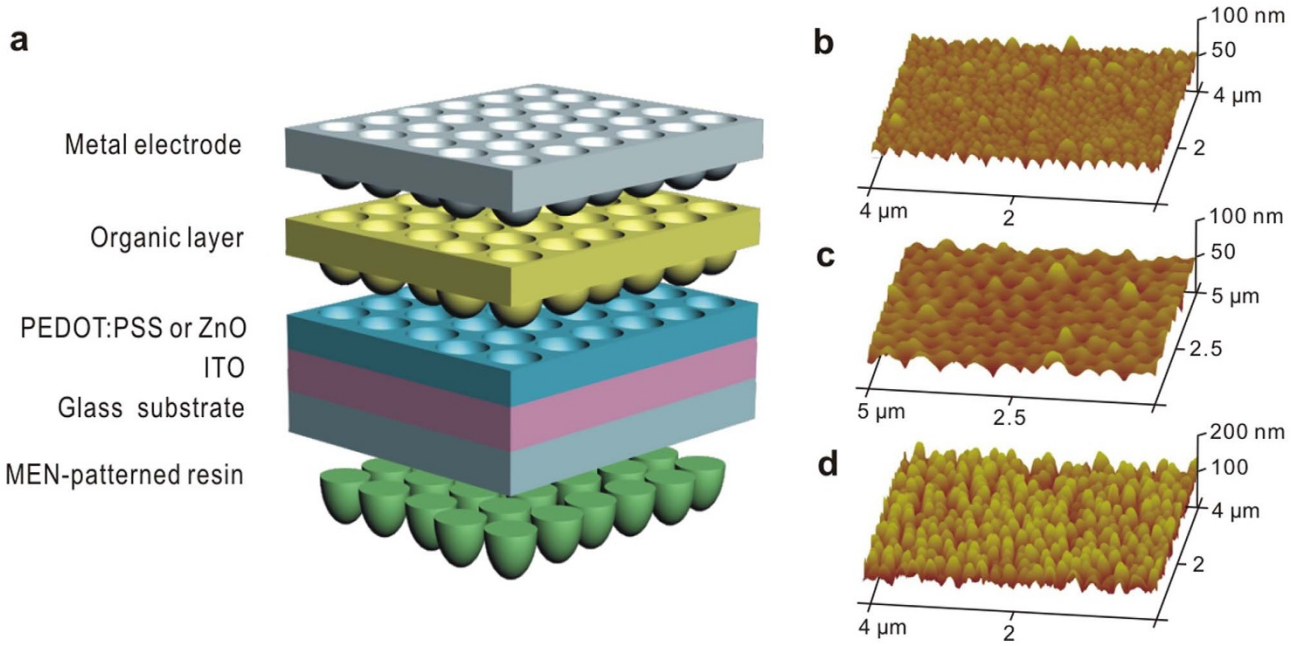

Figure 1 | Device structure and atomic force microscope (AFM) images of moth's eye nanostructure (MEN). (a), Schematic diagram of OLED and OSC integrated with dual-side MENs. Internal MEN is first patterned on a PEDOT:PSS or ZnO layer on ITO coated glass substrate for OLED or OSC, respectively. The organic active layers and metal electrode are then deposited on the corrugated PEDOT:PSS or ZnO layer. Diagram is not to scale. (b), View of internal MEN transferred on PEDOT:PSS layer on ITO surface for OLEDs, showing a period of ~200 nm, a groove depth of ~80 nm, a diameter of ~100 nm, and duty cycle of 0.5. (c), View of internal MEN patterned on ZnO layer on ITO surface for OSCs, showing a period of ~400 nm, a groove depth of 80 nm, a diameter of ~200 nm, and duty cycle of 0.5. (d), View of external MEN patterned on UV-resin on glass surface, showing a period of ~200 nm, a groove depth of 180 nm, a diameter of ~120 nm, and duty cycle of 0.6.

no spectral distortion or any change in device electrical properties. Similarly, the PCE of MEN-patterned OSCs can be enhanced to 9.33% with a 20% increase in short-circuit current density (J_{SC}) without any detrimental changes on open circuit voltages (V_{OC}) and fill factor (FF). We anticipate our findings will stimulate the development of new device structures of much improved efficiency for commercial applications.

Results

MEN fabrication. Figure 1a depicts a schematic diagram of the device structure constructed with dual-side MEN, which was transferred by an imprinting technique using perfluoropolyether (PFPE) mold containing the MEN with compressive stress on the surface of poly(3,4-ethylene dioxythiophene):polystyrene sulfonic acid (PEDOT:PSS), ZnO, or UV-curable resin films supported on ITO glass substrates (see the **Methods** and Supplementary Figs. S1–S5 for the fabrication processes of PFPE molds and devices). Both the sub-wavelength structures and a continuously tapered morphology can be observed on the surface of PFPE molds, which effectively mimic the natural structures of a moth's eyes.

Figure 1b–d present the atomic force micrographs (AFM) of MENs patterned on a PEDOT:PSS layer (Fig. 1b), a ZnO layer (Fig. 1c), as well as UV-curable resin film (Fig. 1d), showing the produced MENs is smaller than visible wavelength. Tapping-mode AFM studies of these layers show that the surface root-mean-square (RMS) roughness of the PEDOT:PSS layer was changed from 1.03 ± 0.01 nm to 5.28 ± 0.05 nm upon the imprinting, while that of the ZnO layer varied from 0.98 ± 0.02 nm to 6.43 ± 0.07 nm. Note that the MEN diameter of imprinted ZnO or PEDOT:PSS layer is smaller than the feature size of the PFPE mold (Supplementary Figs. S2–4), which is attributed to shrinkage of ZnO or PEDOT:PSS volume upon the solvent removal during the imprinting procedure. In addition, the surface morphologies of the deposited organic layers confirm the conformal coating of each functional layer on the patterned PEDOT:PSS or ZnO layer, although deposition of each successive layer causes progressive smoothing of the MEN structuring (Supplementary Fig. S6).

To evaluate the capability of dual-side MEN on light coupling in organic optoelectronics, we constructed OLED and OSC devices using representative materials in a conventional architecture on dual-side MEN-patterned substrates as well as flat substrates (See **Methods** for materials composition and device structures used for OLEDs and OSCs). The device with dual-side MEN is fabricated as shown in Fig. 1a. The conventional device is on a flat substrate without MEN. For device with internal MEN, a MEN is only transferred to the PEDOT:PSS or ZnO layer on top of ITO surface before organic layer deposition. For device with external MEN, the MEN is only transferred to UV-curable resin on the glass surface. To ensure consistent results, each series of all four samples for OLEDs or OSCs were simultaneously fabricated in the same batch.

OLED fabrication with MEN. The performance characteristics of green phosphoresent OLEDs including a multi-photon emission (MPE) structure of single, double or triple electroluminescence (EL) units[47] on four different substrates are compared and plotted in Fig. 2. It is shown that the electrical properties of devices patterned with MEN are almost identical to that on a flat substrate (Fig. 2a), while the luminance is dramatically increased compared to that without MEN (Fig. 2b–d). The EQE (Fig. 2b–d) and current efficiency (Supplementary Fig. S7) for these devices at a luminance of 1,000 cd m^{-2} and the EQE enhancement ratios relative to that of a conventional device are summarized in Table 1. For OLED combining internal MEN and single EL unit, the EQE is 69% higher than that of the conventional device constructed on flat substrate, which corresponds to an increase in the amount of confined light from the organic layers and ITO electrode into the glass substrate[2]. The external MEN promotes the out-coupling of light originally trapped in glass due to total internal reflection, as

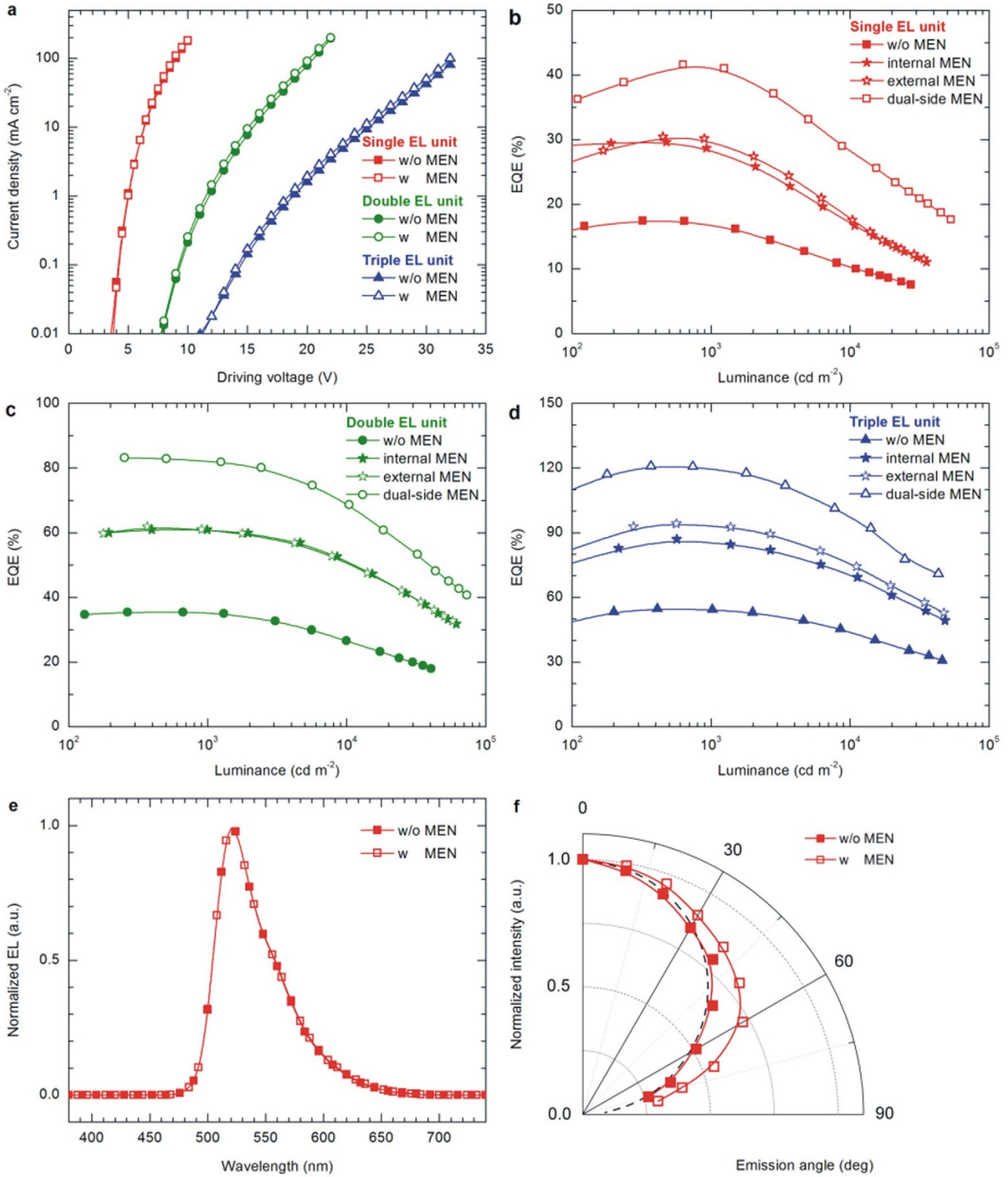

Figure 2 | **Performance characteristics of OLEDs.** (a–d), Current density-voltage (J-V) characteristics (a) and EQE versus luminance (cd m^{-2}) (b–d) of representative OLEDs without MEN (filled symbols) and with dual-side MEN (open symbols), which combine a MPE structure with single (b, squares), double (c, circles), and triple (d, triangles) EL units. Filled and open stars in (b–d) represent the devices only using internal and external MEN, respectively. (e), (f), Normalized EL spectra (e) and angular dependence of light intensities (f) for OLEDs without MEN (filled symbols) and with dual-side MEN (open symbols), measured at J = 1 mA cm^{-2}. The dashed line in (f) represents a guide to the ideal Lambertian emission pattern.

Table 1 | Efficiency comparison for OLEDs with different MENs, measured at 1000 cd m^{-2}

Device type	EQE (%)	Enhancement ratio	Current efficiency[a] (cd A^{-1})
Single EL unit			
Conventional	16.7	1	62.3
Internal MEN	28.2	1.69	92.5
External MEN	29.6	1.77	87.5
Dual-side MEN	41.1	2.46	124.6
Double EL unit			
Conventional	35.1	1	132.4
Internal MEN	60.7	1.73	197.0
External MEN	60.6	1.73	181.5
Dual-side MEN	82.3	2.34	251.0
Triple EL unit			
Conventional	54.3	1	203.8
Internal MEN	85.4	1.57	280.5
External MEN	93.3	1.72	280.3
Dual-side MEN	119.7	2.20	366.0

[a]The current efficiency was estimated only by the luminance at the surface normal.

illustrated by the 77% enhancement in EQE. As illustrated in Table 1, the dual-side MEN enables a further improvement of efficiency by a factor of 2.46 times that of the conventional device without MEN, due to enhanced light extraction from organic layers, ITO as well as glass. The resulting OLED combining dual-side MEN with a MPE structure of triple EL unit yields a maximum EQE of 119.7% and current efficiency of 366 cd A^{-1} at 1,000 cd m^{-2}, which is among the highest values ever reported for OLEDs in the literature[47–49].

To investigate the influence of MEN on light extraction, the normalized EL spectra of devices without and with MEN were measured and shown in Fig. 2e. It is shown that the device with MEN exhibits wavelength-independent enhancement in efficiency, confirming no grating effects with the quasi-periodic sub-wavelength structure. Additionally, unified EL spectra of OLEDs with MEN were obtained, which are independent of the viewing angle, in contrast to the conventional OLED showing a variation of the emission spectra (Supplementary Fig. S8). The angular dependences of light intensity for OLEDs without and with MEN are displayed in Fig. 2f. The emission of the conventional device is close to a Lambertian pattern, whereas the integration of dual-side MEN in OLED causes a stronger side emission, which is mainly due to redirected emission over all azimuthal directions. Similar enhancement was also observed for blue and red OLEDs without spectral distortion (Supplementary Fig. S9), indicating the excellent light manipulation capability of MENs for use in full-color and white OLEDs using only one single patterned structure.

OSC fabrication with MEN. Figure 3a plots the J-V characteristics of OSCs constructed on four different substrates under 100 mW cm^{-2} air mass 1.5 global (AM 1.5 G) illumination, where model polymer constituents of thieno[3,4-b]thiophene/benzodithiophene (PTB7) and [6,6]-phenyl C_{71}-butyric acid methyl ester ($PC_{71}BM$) were used to create the donor-acceptor bulk-heterojunction photoactive layer in the OSCs. The detailed parameters deduced from the J-V characteristics are summarized in Table 2. Regardless of the variation of MEN-patterned substrates, these four OPVs yield almost constant V_{OC} of 0.73 V and FF of ~60%, which are in good agreement with the reported values in the literature[10]. However, the use of internal, external, and dual-side MENs causes large and substantial variations in J_{SC} compared with that of a conventional cell on a flat substrate. Specifically, after incorporation of dual-side MEN the J_{SC} is highly enhanced from 17.59 mA cm^{-2} to 21.15 mA cm^{-2}, corresponding to an enhancement ratio of as high as 20%.

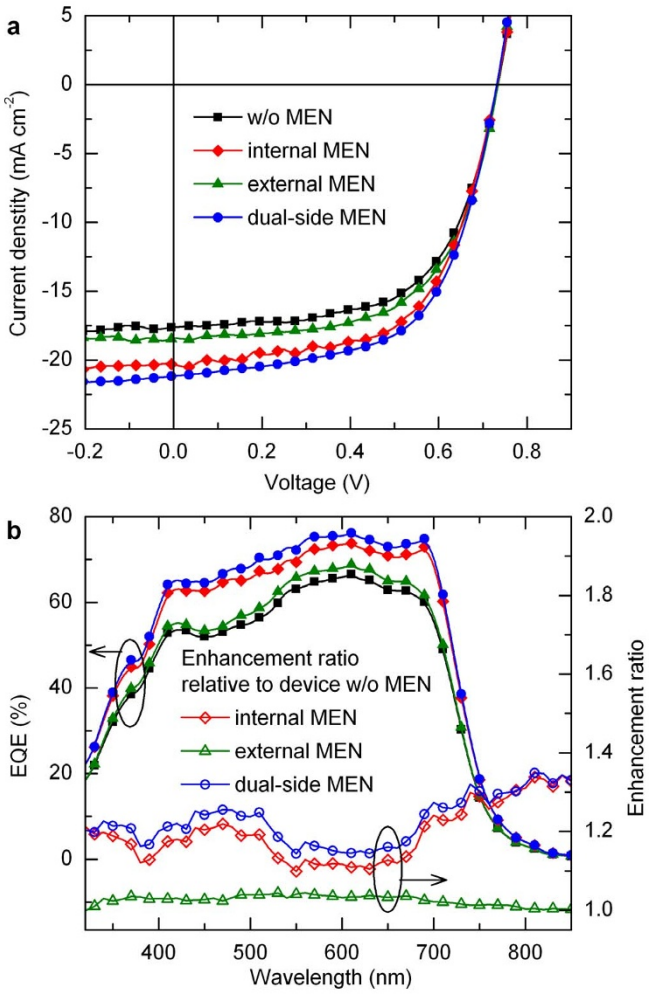

Figure 3 | Photovoltaic performance of OSCs. (a), J-V characteristics of OSCs constructed with a structure of ITO/ZnO/PTB7:$PC_{71}BM$/MoO_3/Al without MEN (squares) and with internal (diamond), external (triangles), and dual-side (circles) MEN, respectively, under 100 mW cm^{-2} AM 1.5 G illumination. (b), The EQE spectra of the corresponding devices and enhancement ratio as a function of emission wavelength, obtained by dividing the spectra of the devices with MEN by that without MEN.

Consequently, a maximum PCE value of 9.33% is obtained, which is among the highest values ever reported to date for OSCs with single photo-active layer[10]. Since the blended PTB7:$PC_{71}BM$ active layers in these four OSCs were prepared during the same batch processing with similar degree of crystallinity, the performance enhancement, especially the increase in J_{SC}, is ascribable to enhanced light harvesting within the active layer of PTB7:$PC_{71}BM$ due to improved light trapping in the active layer after integration of MENs.

To verify the effect of J_{SC} enhancement, the EQE spectra of the corresponding devices are measured and presented in Fig. 3b. The enhancement ratios of EQE spectra relative to that of the conventional cell are also plotted in Fig. 3b to distinguish which part contributed to the enhancement. For the cells only using external MEN, a uniform increase of the spectral response is clearly observed across the wavelength range of 350 nm to 800 nm, which is in agreement with the fact that the MEN can function as an effective anti-reflective layer[44]. The use of internal and dual-side MENs can cause a further EQE enhancement, and the averaged photo-response with dual-side MEN is ~20% enhanced as compared to that on a flat substrate in the wavelength range from 350 nm to 800 nm.

Optical characterization of OLEDs and OSCs with MEN. Figure 4 compares the transmittance of ITO-glass substrates without and with

Table 2 | Photovoltaic parameters for OSCs with different MENs, measured under 100 mW cm^{-2} AM 1.5 G illumination. The average values obtained from at least 24 cells are given in brackets

Device type	PCE (%)	J_{SC} (mA cm^{-2})	V_{OC} (V)	FF (%)
Conventional	7.89 (7.78)	17.59 (17.44)	0.73 (0.73)	61.52 (60.53)
Internal MEN	8.94 (8.75)	20.35 (20.27)	0.73 (0.73)	60.21 (59.21)
External MEN	8.24 (8.10)	18.41 (18.23)	0.73 (0.73)	61.32 (60.42)
Dual-side MEN	9.33 (9.12)	21.15 (20.96)	0.73 (0.73)	60.43 (58.92)

MENs used in OLEDs and OSCs, respectively. The measurements were conducted with the propagation of incident light towards the glass side for OLEDs and towards the ITO side for OSCs, respectively. The broadband optical nature of different MENs patterned on substrates used in OLEDs and OSCs can be observed in Fig. 4. The incorporation of dual-side MEN sustains a high value on transmittance over a wide spectral range of 350–800 nm, which is 7% higher than that of the flat ITO glass. It is also noted that the use of only internal or external MEN leads to an intermediate increase in transmittance compared to that of flat ITO-glass, showing a good match between the transmittance of MEN patterned ITO glass substrate and the experimentally obtained light coupling enhancement in OLEDs and OSCs. The enhancement of optical transmittance over the entire spectrum is attributed to the contributions from the broad distribution of periodicity of the MEN pattern and the gradient refractive index profiles of MENs at the interface[41–44].

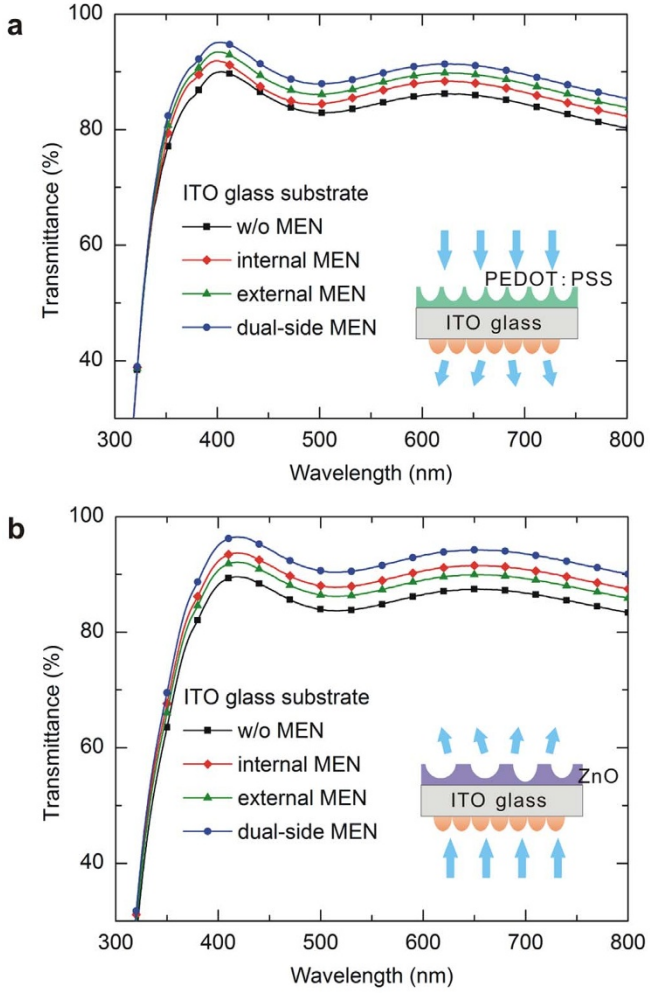

Figure 4 | Optical properties of OLED and OSC with MEN. (a), (b), Transmittance of the incident light from ITO side to PEDOT:PSS-coated OLED substrates (a), and from glass side to ZnO-coated OSC substrates (b) patterned without MEN (squares) and with internal (diamond), external (triangles), and dual-side (circles) MEN. Inset depicts the schematic of the measurement procedure.

To determine the amount of light scattering present in MENs, specular and diffuse transmission measurements for ITO-glass substrates without and with MENs used in OLEDs and OSCs were performed (Supplementary Fig. S10). The transmittance haze (haze = diffuse transmission/total transmission) shows the percentage of total light transmitted that is scattered. The average haze for ITO glass substrates with dual-side MENs used in OLEDs and OSCs are 4.04% and 2.92%, respectively, over the visible spectrum. For comparison, a PEDOT:PSS- or ZnO-coated ITO glass substrate without MEN has negligible haze of ~0.4%. It indicates that scattering is present and significantly contributes to the total transmission.

Simulation of OLEDs and OSCs with MEN. To gain further insight into the optical manipulation of light in OLEDs and OSCs using dual-side MEN, we perform the optical modeling calculations of light propagation using the finite-difference-time-domain (FDTD) method (see **Methods** for the detailed procedure of the optical modeling). Compared to the light that initially undergoes in a conventional OLED (Fig. 5a), dual-side MEN effectively increases the out-coupling probability of the emitted light as observed clearly from the intensity field distribution with propagation not only inside the device but also at the glass/air interface (Fig. 5b). This improvement of light extraction in OLEDs is chiefly attributed to the diffraction grating of the emission layer, corrugated metal electrode, and the gradual transition in refractive index of the UV-curable resin-patterned MEN on the surface of glass substrate. These factors enable the emitted light towards the surface normal with higher out-coupling efficiency[44].

Figure 5c,d display the cross-section field profiles of transverse magnetic (TM) polarized light at 720 nm in OSCs without and with MEN. As shown in Fig. 5c for the device constructed on a flat substrate, the power flux is localized around the PTB7:$PC_{71}BM$ active layer, and quickly decreases towards the Al electrode. On the contrary, the modeled results (Fig. 5d) show that the incorporation of internal MEN patterned on ZnO layer can significantly influence the optical field distribution of incident light within the active layer. The simulation results provide theoretical support to the photonic enhancement of light trapping and absorption in the active layer as well as the PCE enhancement, which is induced not only by a geometric effect on light scattering but also other related causes (e.g., surface plasmonic resonance) from nanostructured active layer and corrugated metal electrode (see the detailed theoretical analysis in Supplementary Fig. S11)[36].

Discussion

As demonstrated here, integrating a dual-side MEN with broadband quasi-omnidirectional properties provides a universal method of light manipulation for use in the performance improvement of organic optoelectronic devices of various material systems. An out-coupling enhancement by a factor of over 2 times that using a conventional flat glass substrate is realized in OLEDs, resulting in significant improvement of EQE to 119.7% and current efficiency to 366 cd A^{-1} at a luminance of 1,000 cd m^{-2}. The 20% enhancement of

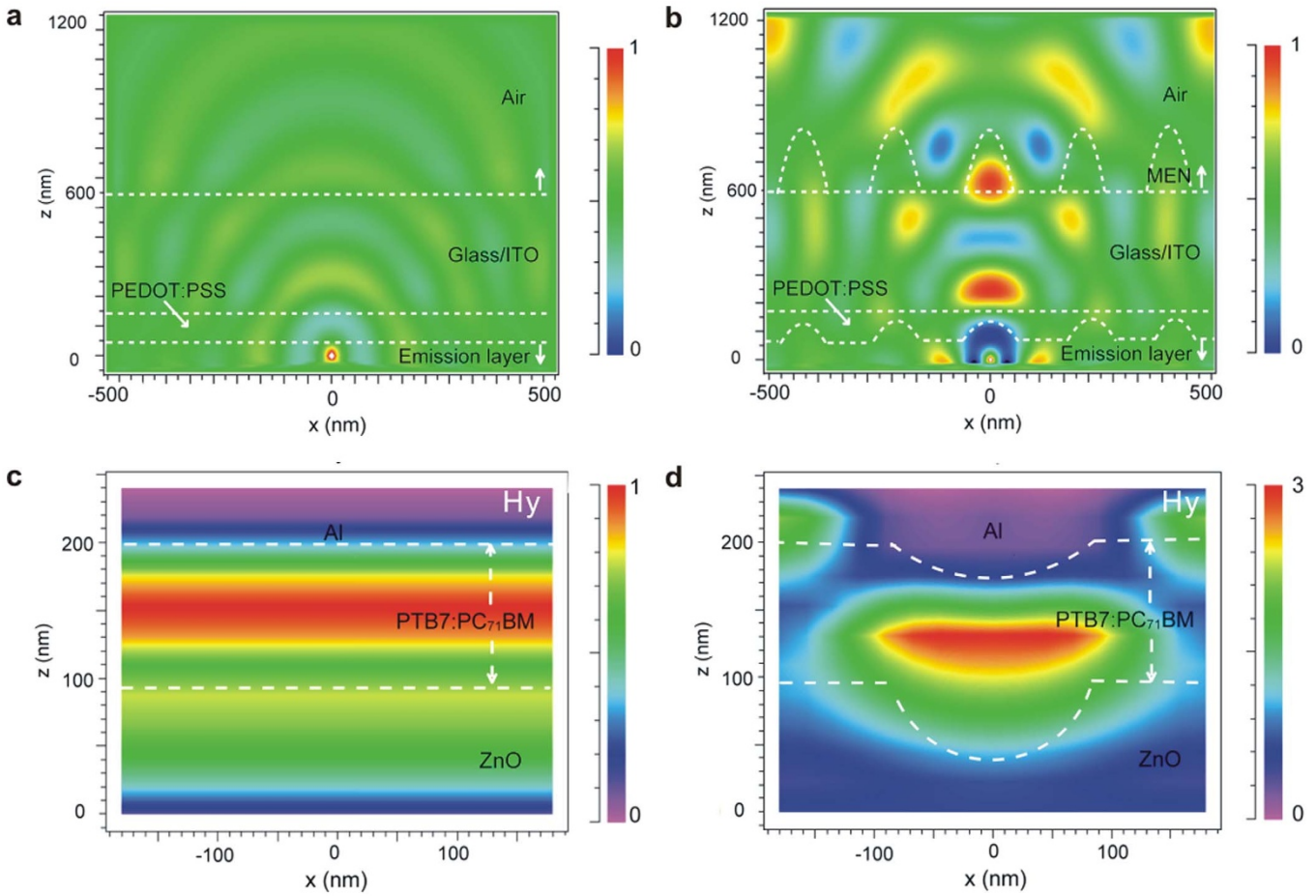

Figure 5 | Simulation of OLED and OSC with MEN. (a), (b), Normalized cross-section intensity field distributions with propagation of OLEDs without (a) and with (b) MEN-patterned PEDOT:PSS layer using Finite Difference Time Domain (FDTD) method (Rsoft FullWave). (c), (d), Normalized cross-section magnetic field profiles of TM polarized light at 720 nm for OSC without (c) and with (d) MEN-patterned ZnO layer.

light harvesting yields a highly efficient OSC with an efficiency of 9.33%. It has been found that both the morphology and the dimensions of the nanostructure in biomimetics are critical to produce the desired functionality[50]. The light coupling enhancement in OLEDs and OSCs with MEN is the combined result of both the two-dimensional sub-wavelength structures and the continuously tapered morphology on the patterned surface with a superior gradient refractive index profile at the interface. The light is therefore manipulated in all azimuthal directions over the entire emission wavelength range. The optical simulations provide an understanding of optical manipulation of light out-coupling and in-coupling process in OLEDs and OSCs. Note also that the method developed here brings about an invaluable advantage, which enables the processing compatibility with the high-throughput large-area roll-to-flat and roll-to-roll manufacturing techniques in future mass production of low-cost organic optoelectronic devices.

Methods

Nanoimprint lithography of mens and characterization. The MENs were fabricated by nanoimprint lithography. PFPE molds containing different MEN were used to perform the imprinting on both sides of ITO-patterned glass substrate with a sheet resistance of 20 Ω per square. For the fabrication of OLED devices, the ITO-patterned glass substrate was spin-coated by the aqueous PEDOT:PSS solution. For the case of OSCs, the sol-gel-derived ZnO layer was formed on ITO glass substrate through spin-coating of the ZnO precursor solution, which was prepared by dissolving 0.5 M zinc acetate dehydrate ($Zn(CH_3COO)_2 \cdot 2H_2O$, Alfa Aeser, 99.5%, 220 mg) in the solvent consisting of ethanolamine ($NH_2CH_2CH_2OH$, Amethyst Chenmicals, 99.5%, 0.061 mL) and 2-methoxyethanol ($CH_3OCH_2CH_2OH$, Alfa Aeser, 99.5%, 2 mL) under vigorous stirring for 12 h for the hydrolysis reaction at ambient conditions. Prior to the molding, the originally spin-coated PEDOT:PSS and ZnO layers were annealed in ambient air at 140°C for 10 min and 150°C for 5 min, respectively. Then, the PFPE mold was put in comformal contact with a 100 nm-thick PEDOT:PSS or ZnO layer, and pressed under a constant pressure of 1.5 bar for 3 min at 140°C. For ensuring the complete formation of a uniform nanohoneycomb morphology on the PEDOT:PSS or ZnO layer, the substrates were annealed for further 9 min at the same temperature after the mold was peeled off. The organic layer and metal electrode were subsequently deposited on the substrate through thermal evaporation or spin-coating to complete the device. Finally, the second UV-assisted imprinting of MEN on the glass surface, which was coated with UV-curable resin, was repeated with a negative PFPE mold after encapsulating the devices with a cap glass to prevent the damage to the formed nanostructures under pressure. The UV resin drop-casted on the glass surface was embossed with a negative PFPE mold under a constant pressure of 1.5 bar for 10 s with a UV illumination at light power intensity of 500 mJ cm^{-2} at a wavelength of 395 nm. The imprinting recipe was optimized by a systematic study of the imprinting time and pressure.

Optical transmittance measurements were carried out using an UV/vis/near-IR spectrometer (Perkin Elmer Lambda 750). Surface morphology of MENs was characterized with AFM (Veeco Multimode V) in the tapping mode. The refractive index of the MEN-patterned films was determined by the alpha-SE™ Spectroscopic Ellipsometer with the angle of incidence at 70°.

OLED fabrication and measurement. For the OLED fabrication, organic layers and metal cathode were thermally deposited in high vacuum chamber with a base pressure of 2×10^{-6} Torr, in which the deposition rate and film thickness were monitored by a quartz crystal oscillator. The OLEDs were composed of a MPE structure of one to three consecutive green phosphorescent EL units, which were electrically connected in series by a bilayer intermediate connector of a 10 nm-thick Mg-doped 4,7-diphenyl-1,10-phenanthroline (Mg:BPhen) and a 5 nm-thick MoO_3. The EL unit consisted of a 40 nm-thick hole-transporting layer of 4,4-bis[N-(1-naphthyl)-N-phenyl-amino]biphenyl (NPB), a 20 nm-thick green emitting layer of 4′-bis(carbazol-9-yl)biphenyl (CBP) doped with bis(2-phenylpyridine)(acetylacetonate)iridium(III) [$Ir(ppy)_2(acac)$, 8 wt%], and a 40 nm-thick electron-transporting/exciton blocking layer of

2,2′,2″-(1,3,5-benzinetriyl)-Tris(1-phenyl-1-H-benzimidazole) (TPBi). This was followed by 0.5 nm-thick LiF and 100 nm-thick Al layers as a bilayer cathode, which was deposited through a shadow mask.

The current density-luminance-voltage (J-L-V) characteristics and EL spectra of OLEDs were measured simultaneously in the forward direction using a programmable source meter (Keithley 2400) and a luminance meter/spectrometer (PhotoResearch PR655) in air ambience. The angular emission patterns were measured by integrating the EL spectra of the devices according to emission angles.

OSC fabrication and measurement. The OSCs were constructed with a structure of ITO/ZnO (100 nm)/PTB7:$PC_{71}BM$ (1 : 1.5 by weight, 100 nm)/MoO_3 (10 nm)/Al (100 nm). PTB7 and $PC_{71}BM$ were purchased from 1-material Chemscitech and Lumitec, respectively, and used as received. After the preparation of ZnO layer without or with MEN, the substrates were transferred into nitrogen-filled glove box for the active layer coating. The PTB7:$PC_{71}BM$ active blend layer was prepared by spin-coating the solution of PTB7:$PC_{71}BM$ in chlorobenzene/1,8-diiodoctane (97 : 3% by volume) mixed solvent (concentration, 25 mg mL^{-1}) at 1000 rpm for 2 min on top of the ZnO layer and dried in vacuum, forming a nominal thickness of ~100 nm. To complete device fabrication, a 10 nm MoO_3 layer and a 100 nm Al layer were subsequently evaporated to form a top anode. A shadow mask was used to define the Al anode, determining the device area of 0.1 cm^2.

The photovoltaic characteristics of OSCs were examined in air at room temperature using a programmable Keithley 2612 source measurement unit under a 1 sun, AM 1.5 G spectrum from a solar simulator (Oriel model 91160; 100 mW m^{-2}). The EQE measurement was conducted with a photo-modulation spectroscopic setup (Newport monochromator). The illumination intensity of solar simulator was calibrated using a standard Si reference cell with known spectral response.

Optical modeling and simulation. The optical properties for OLEDs and OSCs were theoretically determined by 3 dimensional modeling with commercial RSoft 8.1 (RSoft Design Group, Inc), in which hexagonal closely packed nanostructures with linearly tapered profile were used for simplicity instead of randomly distributed geometry. For simulation of light out-coupling in OLEDs, the FDTD method (RSoft Fullwave) was performed to investigate the light transmission characteristics. For characterizing light absorption in OSCs, the rigorous coupled wave analysis (RCWA) (RSoft DiffractMOD) was employed to solve Maxwell's equations for electromagnetic modes present in each layer after introduction of MEN. A plane-wave source was directed along the z-axis to calculate their transmittance properties. The extinction coefficients and complex refractive indices of n and k of all layers used in the simulation were experimentally obtained by spectroscopic ellipsometer measurement.

1. Reineke, S. *et al.* White organic light-emitting diodes with fluorescent tube efficiency. *Nature* **459**, 234–238 (2009).
2. Sun, Y. & Forrest, S. R. Enhanced light out-coupling of organic light-emitting devices using embedded low-index grids. *Nature Photon.* **2**, 483–487 (2008).
3. Koo, W. H. *et al.* Light extraction from organic light-emitting diodes enhanced by spontaneously formed buckles. *Nature Photon.* **4**, 222–226 (2010).
4. Uoyama, H., Goushi, K., Shizu, K., Nomura, H. & Adachi, C. Highly efficient organic light-emitting diodes from delayed fluorescence. *Nature* **492**, 234–238 (2012).
5. Dou, L. T. *et al.* Tandem polymer solar cells featuring a spectrally matched low-bandgap polymer. *Nature Photon.* **6**, 180–185 (2012).
6. Park, S. H. *et al.* J. Bulk heterojunction solar cells with internal quantum efficiency approaching 100%. *Nature Photon.* **3**, 297–302 (2009).
7. Kim, J. B. *et al.* Wrinkles and deep folds as photonic structures in photovoltaics. *Nature Photon.* **6**, 327–332 (2012).
8. Sun, Y. M. *et al.* Solution-processed small-molecule solar cells with 6.7% efficiency. *Nature Mater.* **11**, 44–48 (2012).
9. Brabec, C. J. *et al.* Polymer-fullerene bulk-heterojunction solar cells. *Adv. Mater.* **22**, 3839–3856 (2010).
10. He, Z. *et al.* Enhanced power-conversion efficiency in polymer solar cells using an inverted device structure. *Nature Photon.* **6**, 591–595 (2012).
11. Baldo, M. A. *et al.* Highly efficient phosphorescent emission from organic electroluminescent devices. *Nature* **395**, 151–154 (1998).
12. Goushi, K., Yoshida, K., Sato, K. & Adachi, C. Organic light-emitting diodes employing efficient reverse intersystem crossing for triplet-to-singlet state conversion. *Nature Photon.* **6**, 253–258 (2012).
13. Williams, E. L., Haavisto, K., Li, J. & Jabbour, G. E. Excimer-based white phosphorescent organic light-emitting diodes with nearly 100 % internal quantum efficiency. *Adv. Mater.* **19**, 197–202 (2007).
14. Jo, J. *et al.* Three-dimensional bulk heterojunction morphology for achieving high internal quantum efficiency in polymer solar cells. *Adv. Funct. Mater.* **19**, 2398–2406 (2009).
15. Hobson, P. A., Wedge, S., Wasey, J. A. E., Sage, I. & Barnes, W. L. Surface plasmon mediated emission from organic light-emitting diodes. *Adv. Mater.* **14**, 1393–1396 (2002).
16. Bulović, V. *et al.* Weak microcavity effects in organic light-emitting devices. *Phys. Rev. B* **58**, 3730–3740 (1998).
17. Smith, L. H., Wasey, J. A. E., Samuel, I. D. W. & Barnes, W. L. Light out-coupling efficiencies of organic light-emitting diode structures and the effect of photoluminescence quantum yield. *Adv. Funct. Mater.* **15**, 1839–1844 (2005).
18. Chutinan, A., Ishihara, K., Asano, T., Fujita, M. & Noda, S. Theoretical analysis on light-extraction efficiency of organic light-emitting diodes using FDTD and mode-expansion methods. *Org. Electron.* **6**, 3–9 (2005).
19. Liang, Y. Y. *et al.* For the bright future—bulk heterojunction polymer solar cells with power conversion efficiency of 7.4%. *Adv. Energy Mater.* **22**, E135–E138 (2010).
20. Xu, Z. Q. *et al.* Enhanced performance in polymer photovoltaic cells with chloroform treated indium tin oxide anode modification. *Appl. Phys. Lett.* **98**, 253303 (2011).
21. Blouin, N. *et al.* Toward a rational design of poly(2,7-carbazole) derivatives for solar cells. *J. Am. Chem. Soc.* **130**, 732–742 (2008).
22. Cho, N. *et al.* n-Doping of thermally polymerizable fullerenes as an electron transporting layer for inverted polymer solar cells. *J. Mater. Chem.* **21**, 6956–6961 (2011).
23. Li, X. H. *et al.* Dual plasmonic nanostructures for high performance inverted organic solar cells. *Adv. Mater.* **24**, 3046–3052 (2012).
24. Na, S. I. *et al.* Efficient polymer solar cells with surface relief gratings fabricated by simple soft lithography. *Adv. Funct. Mater.* **18**, 3956–3963 (2008).
25. Bai, Y. *et al.* Outcoupling of trapped optical modes in organic light-emitting devices with one-step fabricated periodic corrugation by laser ablation. *Org. Electron.* **12**, 1927–1935 (2011).
26. Cho, K. H., Ahn, S. I., Lee, S. M., Choi, C. S. & Choi, K. C. Surface plasmonic controllable enhanced emission from the intrachain and interchain excitons of a conjugated polymer. *Appl. Phys. Lett.* **97**, 193306 (2010).
27. Kwon, M. K. *et al.* Surface-plasmon-enhanced light-emitting diodes. *Adv. Mater.* **20**, 1253–1257 (2008).
28. Koh, T. W., Choi, J. M., Lee, S. & Yoo, S. Optical outcoupling enhancement in organic light-emitting diodes: highly conductive polymer as a low-index layer on microstructured ITO electrodes. *Adv. Mater.* **22**, 1849–1853 (2010).
29. Möller, S. & Forrest, S. R. Improved light out-coupling in organic light emitting diodes employing ordered microlens arrays. *J. Appl. Phys.* **91**, 3324–3327 (2002).
30. Wei, M. K. & Su, I. L. Method to evaluate the enhancement of luminance efficiency in planar OLED light emitting devices for microlens array. *Opt. Express* **12**, 5777–5782 (2004).
31. Yang, J. P. *et al.* Light out-coupling enhancement of organic light-emitting devices with microlens array. *Appl. Phys. Lett.* **97**, 223303 (2010).
32. Kim, J. Y. *et al.* New architecture for high-efficiency polymer photovoltaic cells using solution-based titanium oxide as an optical spacer. *Adv. Mater.* **18**, 572–576 (2006).
33. Chen, F. C., Wu, J. L. & Hung, Y. Spatial redistribution of the optical field intensity in inverted polymer solar cells. *Appl. Phys. Lett.* **96**, 193304 (2010).
34. Ko, D. H. *et al.* Photonic crystal geometry for organic solar cells. *Nano Lett.* **9**, 2742–2746 (2009).
35. Sergeant, N. P. *et al.* Design of transparent anodes for resonant cavity enhanced light harvesting in organic solar cells. *Adv. Mater.* **24**, 728–732 (2012).
36. Atwater, H. A. & Polman, A. Plasmonics for improved photovoltaic devices. *Nature Mater.* **9**, 205–213 (2010).
37. Cheng, P. P. *et al.* Plasmonic backscattering enhancement for inverted polymer solar cells. *J. Mater. Chem.* **22**, 22781–22787 (2012).
38. Kang, M. G., Xu, T., Park, H. J., Luo, X. & Guo, L. J. Efficiency enhancement of organic solar cells using transparent plasmonic Ag nanowire electrodes. *Adv. Mater.* **22**, 4378–4383 (2010).
39. Kulkarni, A. P., Noone, K. M., Munechika, K., Guyer, S. R. & Ginger, D. S. Plasmon-enhanced charge carrier generation in organic photovoltaic films using silver nanoprisms. *Nano Lett.* **10**, 1501–1505 (2010).
40. Wang, D. H. *et al.* Enhanced power conversion efficiency in PCDTBT/PC70BM bulk heterojunction photovoltaic devices with embedded silver nanoparticle clusters. *Adv. Energy Mater.* **1**, 766–770 (2011).
41. Huang, Y. F. *et al.* Improved broadband and quasi-omnidirectional anti-reflection properties with biomimetic silicon nanostructures. *Nature Nanotechnol.* **2**, 770–774 (2007).
42. Cai, J. *et al.* Self-cleaning, broadband and quasi-omnidirectional antireflective structures based on mesocrystalline rutile TiO2 nanorod arrays. *Energy Environ. Sci.* **5**, 7575–7581 (2012).
43. Ravipati, S. *et al.* Broadband and wide angle antireflection of sub-20 nm GaAs nanograss. *Energy Environ. Sci.* **5**, 7601–7605 (2012).
44. Raut, H. K. *et al.* Robust and durable polyhedral oligomeric silsesquioxane-based anti-reflective nanostructures with broadband quasi-omnidirectional properties. *Energy Environ. Sci.* **6**, 1929–1937 (2013).
45. Sainiemi, L. *et al.* Non-reflecting silicon and polymer surfaces by plasma etching and replication. *Adv. Mater.* **23**, 122–126 (2011).
46. Diedenhofen, S. L. *et al.* Broad-band and omnidirectional antireflection coatings based on semiconductor nanorods. *Adv. Mater.* **21**, 973–978 (2009).
47. Chiba, T. *et al.* Ultra-high efficiency by multiple emission from stacked organic light-emitting devices. *Org. Electron.* **12**, 710–715 (2011).
48. Wang, Z. B. *et al.* Unlocking the full potential of organic light-emitting diodes on flexible plastic. *Nature Photon.* **5**, 753–757 (2011).

49. Kim, J. B., Lee, J. H., Moon, C. K., Kim, S. Y. & Kim, J. J. Highly enhanced light extraction from surface plasmonic loss minimized organic light-emitting diodes. *Adv. Mater.* **25**, 3571–3577 (2013).
50. Lee, L. P. & Szema, R. Inspirations from biological optics for advanced photonic systems. *Science* **310**, 1148–1150 (2005).

Acknowledgments

J.T., Y.L., S.S. and S.L. acknowledge financial support from the National Basic Research Program of China (Grant No. 2014CB932600), the National Nature Science Foundation of China (Nos 61007020, 91027041, 61107022, 61036009), Jiangsu Province Natural Science Foundation (No.10KJA140048), and the project of the Priority Academic Program Development (PAPD) of Jiangsu Higher Education Institutions.

Author contributions

J.T. and Y.L. conceived the idea and designed the experiments. L.Z. designed the patterned structure and performed the optical simulation. Q.O. fabricated and characterized the OLED devices. J.C. fabricated and characterized the OSC devices. S.S. performed the fabrication of nanostructured molds. S.L. discussed and interpreted the results. Y.L. analyzed most of the data and wrote the manuscript. J.T. motivated this work and co-wrote the manuscript with input from the other authors. All authors were involved in extensive discussions and data analyses.

Additional information

Supplementary information accompanies this paper at http://www.nature.com/scientificreports

Competing financial interests: The authors declare no competing financial interests.

How to cite this article: Zhou, L. *et al.* Light Manipulation for Organic Optoelectronics Using Bio-inspired Moth's Eye Nanostructures. *Sci. Rep.* **4**, 4040; DOI:10.1038/srep04040 (2014).